Optimizing Piezoelectric Cantilever Design for Electronic Nose Applications

Matiyas Tsegay Korsa [1,*] ![ORCID]**, Josep Maria Carmona Domingo** [2] ![ORCID]**, Lawrence Nsubuga** [3]**,
Jeanette Hvam** [3]**, Florian Niekiel** [4]**, Fabian Lofink** [4]**, Horst-Günter Rubahn** [2] ![ORCID]**, Jost Adam** [1] ![ORCID]
and Roana de Oliveira Hansen [2,*] ![ORCID]

[1] Department of Mechanical and Electrical Engineering, University of Southern Denmark,
   Alsion 2, 6400 Sønderborg, Denmark; jostadam@sdu.dk

[2] Mads Clausen Institute, University of Southern Denmark, Alsion 2, 6400 Sønderborg, Denmark;
   josep.95@hotmail.com (J.M.C.D.); rubahn@mci.sdu.dk (H.-G.R.)

[3] AmiNIC ApS, Algade 56, 5500 Middelfart, Denmark; lawrence@mci.sdu.dk (L.N.); jh@aminic.dk (J.H.)

[4] Fraunhofer Institute for Silicon Technology ISIT, Fraunhoferstr. 1, 25524 Itzehoe, Germany;
   florian.niekiel@isit.fraunhofer.de (F.N.); fabian.lofink@isit.fraunhofer.de (F.L.)

[*] Correspondence: matiyas@sdu.dk (M.T.K.); roana@mci.sdu.dk (R.d.O.H.)

![check for updates]

Abstract: This work demonstrates a method to optimize materials and dimensions of piezoelectric cantilevers for electronic nose applications via finite element analysis simulations. Here we studied the optimum piezoelectric cantilever configuration for detection of cadaverine, a biomarker for meat ageing, to develop a potential electronic nose for the meat industry. The optimized cantilevers were fabricated, characterized, interfaced using custom-made electronics, and tested by approaching meat pieces. The results show successful measurements of cadaverine levels for meat pieces with different ages, hence, have a great potential for applications within the meat industry shelf-life prediction.

Keywords: piezoelectric cantilevers; electronic nose; cadaverine; meat aging; biomarker; sensor

1. Introduction

The meat and fish industries are the most massive resource-needing production within the food sector. It is the food-related-branch that results in the highest level of CO_2 emissions, due to among others, deforestation for cattle production and overfishing [1]. The research in household food and drink waste in Europe shows that 32% avoidable waste attributed to not-used in time because of the date labels were not cited [2]. A market study on Europe's food wast reports 10% of avoidable food waste is from meat and fish products, and 10–32% of the wast is due to date labels [3]. Today, households, restaurants, catering and food stores rely on the printed expiration date, which based on general prediction curves for meat degradation. For example, the prediction curve shows that tuna cuts within eight $(+/-)$ 3 days at 5 °C under aerobic conditions. Accordingly, to be on the safe side, expiration dates are set to five days. The only way to control the actual freshness of meat products are microbiological tests conducted at external laboratories requiring shipping of samples, growing and counting bacteria. These tests are carried out seldomly because they are expensive, time-consuming and do not predict the exact expiration date.

Cadaverine is a volatile biogenic amine providing an exact measure for meat spoilage level. The amount of cadaverine gas released by the meat sample increases in a predictable way over time, depending on the type of meat [4–11]. There are cadaverine detection methods available [12,13], but they all need to be carried out at external laboratories, e.g., measurement of cadaverine levels using gas chromatography-mass spectrometry [14]. However, the emerging approach of electronic

nose or electronic tongue in a gas, bio, and chemical sensing can be employed [15–18]. In this regard, microcantilever-based sensors are widely used for low-level gas sensing, and are a good alternative for sensing cadaverine. When a cadaverine molecule binds to a microcantilever, it increases the cantilever beam mass. As a result, it reduces the cantilever beam mechanical resonance frequencies. Therefore, the presence of a few molecules can be detected by changes in the resonance frequencies as well as impedance output variations from dynamic actuation of the piezoelectric driven cantilevers [19–21]. The piezoelectric cantilever beam voltage output and the resonance frequency can be optimized through modeling techniques for improved performance [22]. We have previously conducted studies about cadaverine binding to functionalised cantilever surfaces [23–25].

In this paper, optimum cantilever dimensions and materials for achieving the highest cadaverine detection sensitivity, using the previously studied surface binder, are investigated. Studies on developed cantilevers have shown that the optimum first mode cantilever resonance frequency is in the range of 10–12 kHz in order to maintain linearity to mass response while keeping the cantilever area large enough for optimal cadaverine binding sites. Cantilevers with optimized materials were morphologically characterized by X-ray tomography and ion-beam microscopy, while sensor signal output characterized by electrical impedance measurements. The cantilevers were tested by measuring cadaverine levels on meat samples, and it showed promising results.

2. Methods

To optimize the cantilever dimensions regarding a specific resonance frequency, we performed finite-element method (FEM) simulations, coupled to a bound constraint quadratic optimization routine. We ran the simulations using a commercial finite-element solver, COMSOL Multiphysics, for solving the cantilever's eigenvalue problem to obtain the structure resonance frequency. To further enhance the study, we implemented the stationary piezoelectric effect, solving the model's coupled electrostatics and mechanics problem: applying an electric potential to the piezoelectric material causes a mechanical deformation.

The undamped system motion is defined by Equation (1)

$$\mathbf{M\ddot{u}} + \mathbf{K\dot{u}} = \mathbf{0}, \tag{1}$$

where $\mathbf{M}$ and $\mathbf{K}$ are the cantilever beam mass and stiffness matrix, respectively, depending on the geometric parameters, and $\mathbf{u}$ is the displacement vector. Inserting a solution $\mathbf{u} = \mathbf{v}e^{\lambda t}$, with $\lambda = i\omega_k$, for the corresponding eigenvector $\mathbf{v}$ and natural frequencies $\omega_k \in \{\omega_1, \ldots, \omega_n\}$, for n mode shapes, Equation (1) becomes an eigenvalue problem of the form:

$$(\lambda^2 \mathbf{M} + \mathbf{K})\mathbf{v} = \mathbf{0}. \tag{2}$$

We started the cantilever geometry optimization with the layers' initial geometric parameters, to investigate the cantilever's length and width effect on its resonance frequency. Finally, we investigated the effect of varying various layer thicknesses, while fixing the cantilever beam length and width. Based on the results obtained, the parameters were tuned to get the desired frequency, using the following bound-constrained optimization formulation:

$$\min_{x_i} |\omega_d - \omega(x_i)|,$$
$$\text{subject to } \mathrm{lb}_i \leq x_i \leq \mathrm{ub}_i, \tag{3}$$

where ω_d is desired resonance frequency, $\omega(x_i)$ is cantilever beam eigenfrequency, obtained from the FEM solution of Equation (2), x_i are geometric parameters for $i = 0, 1, 2, 3, \ldots n$, with n geometric parameters, and lb_i and ub_i are the sets of parameter lower and upper bounds, respectively. To minimize the objective function of Equation (3), we used the gradient-free bound optimization by

quadratic approximation (BOBYQA) algorithm, recommended for optimizing parameters affecting the mesh [26].

Figure 1 shows the required layers for a functional dynamically actuated piezoelectric micro-cantilever sensor. The cantilever body consists of polysilicon buried in layers of silicon oxide for electrical insulation. The bulk silicon wafer body supports the cantilever. On the cantilever top, we implemented a piezoelectric layer, in contact with the top and bottom metal electrodes. The whole system insulated by silicon nitride passivation layer, and metallic contacts (Al/Cu) fabricated—both for the bottom and top electrodes. These contacts are wire-bonded to a small printed circuit board, which accommodates the microcantilever chip.
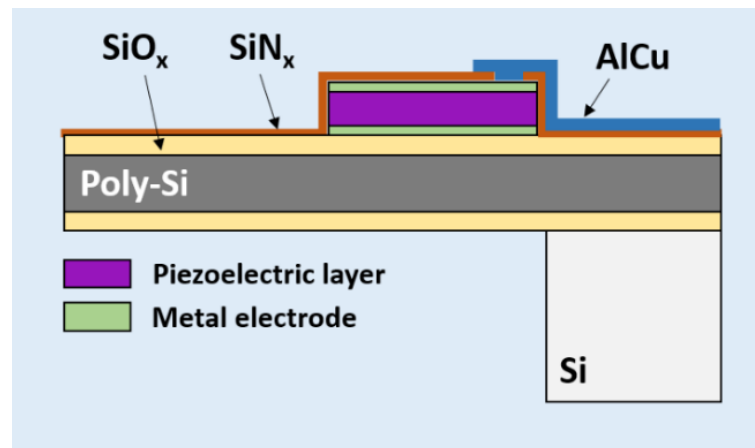

Figure 1. Piezoelectric cantilever cross-section layout, with the description of material layers.

The COMSOL model was implemented with a fixed ends at the silicon block as mechanical boundary condition and a ground at the bottom electrode layer for electrostatic simulation. Then, we simplified it by avoiding the vertical column of aluminium contact and silicon nitride, which has a negligible effect on the result but introduces high aspect ratio domains. The simplified model meshed using hexahedra, and quad as discretizing elements. Figure 2 shows the course and the fine model partitioning whereby longitudinal mesh size used for controlling the result convergence.
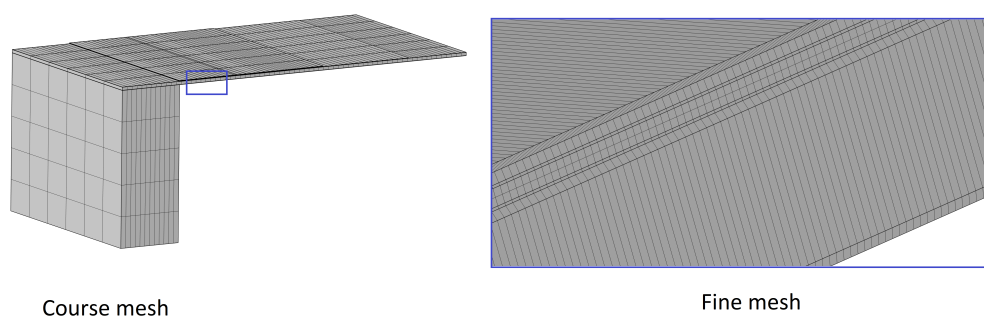

Figure 2. Longitudinally controlled partitioning for meshing the cantilever beam to achieve convergence with the minimum number of elements.

Cantilevers with the desired resonance frequency and a surface area were fabricated at the cleanroom facilities at the Fraunhofer Institute for Silicon Technology, using conventional photolithography, layer deposition, lift-off, and etching processes. First, the metal bottom electrodes are defined by photolithography, followed by metal deposition and lift-off. The recipe involved deposition of AlN piezoelectric layer by sputtering, top and bottom electrode deposition. The silicon nitride passivation layer was finally defined and deposited by sputtering. Lastly, the top and bottom etching of silicon oxide and silicon layers done by chemical etching. The resulting cantilevers morphology

characterized using a Bruker Skyscan X-ray Nano-tomograph and a Zeiss ORION NanoFab Helium Ion Microscope. A 4294A Precision Impedance Analyzer was used to test the performance of the piezoelectric layer, based on the Butterworth Van Dyke model and characterized from the resulting impedance profile.

3. Results and Discussion

Before getting into the geometric parameters versus resonance frequency investigation, it is important to observe the simulation convergence for the accurate result. In this regard, we performed eigenfrequency and electric potential convergence study against the mesh.

Figure 3a shows that a 1 k partitions in the longitudinal direction is enough to converge the first mode resonance frequency. When it comes to the convergence of average potential difference in the piezoelectric material, more partition, around 2 k, is required, as shown in Figure 3b. For the 2 k number of partitions, the number of elements for the whole model is 109865, and the mesh average quality is 0.8969. Hence, the cantilever's partitioning in a longitudinal direction can converge the result with the computationally economic resource. After setting the mesh, we proceed to simulate a stationary study of the cantilever's piezoelectric deformation by the applied voltage. Table 1 shows the parameters used for this initial simulation. We applied 3 V to the top electrode and 0 V to the bottom electrode, sandwiching piezoelectric material, as shown in Figure 4. Figure 5 shows that the cantilever deformation in μm, and the shape of deformation can give insight into what kind of mode shape can be excited by this effect.
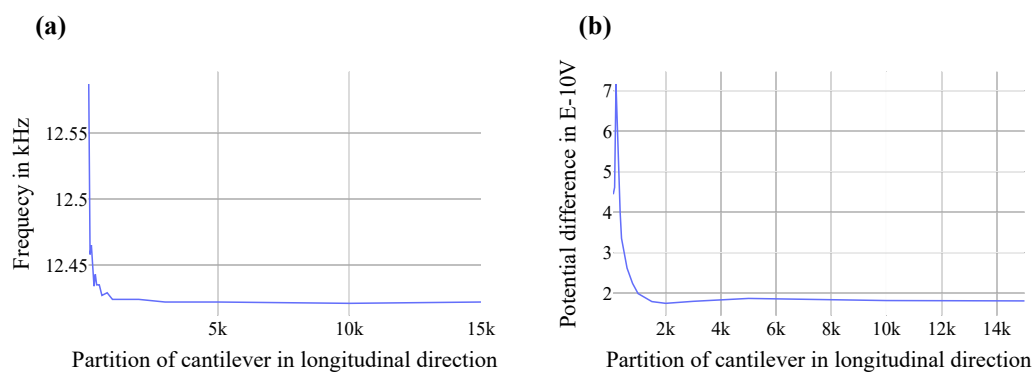
(a)   **(b)**

Figure 3. (**a**) Convergence study for the cantilever beam first mode resonance frequency versus the number of partitioning, showing convergence for less than 2 k number of partition. (**b**) Convergence study for the average potential difference in piezoelectric material versus the number of partitioning, showing convergence around 2 k number of partitioning.

Table 1. Initial parameters used for simulation of stationary study on piezoelectric effect as well as the effect of width and length on cantilever resonance frequency.

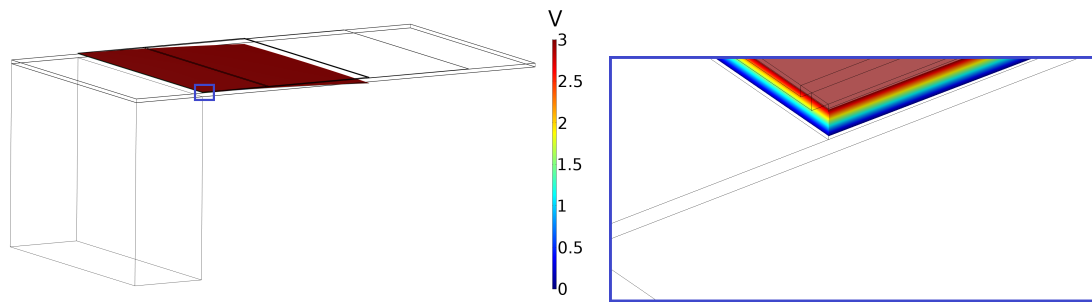| Parameter	Value
Cantilever length	1800 μm
Cantilever width	1000 μm
Cantilever body thickness	14 μm
Metal electrode thickness	0.25 μm
Piezoelectric layer thickness	1.5 μm
Piezoelectric layer material	Aluminum Nitride (AlN)
Metal electrode material	Gold (Au)

Figure 4. Distribution of applied electric potential on piezoelectric material to simulate the cantilever beam deformation.
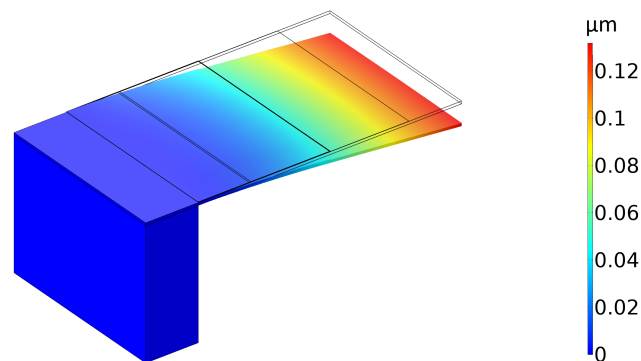

Figure 5. An applied electric field on electrodes causing simple bending on cantilever beam due to piezoelectric effect to compare with cantilever beam resonance frequency mode shapes.

Consequent to the piezoelectric effect stationery study on the cantilever beam, we performed the model's eigenfrequency study, aimed at optimizing the dimensions for getting the resonance frequency in a desirable range. A frequency of 10 kHz as a reference used to solve the first three mode shapes around the referred frequency. We performed the preliminary simulations to have a view of the resultant mode shapes. Figure 6 shows the three mode shapes around the reference frequency. From the shapes, the first mode is similar to the piezoelectric effect's stationary deformation, implying that the applied voltage is adequate to excite this mode. Figure 7 shows the corresponding potential difference for the first mode resonance frequency.
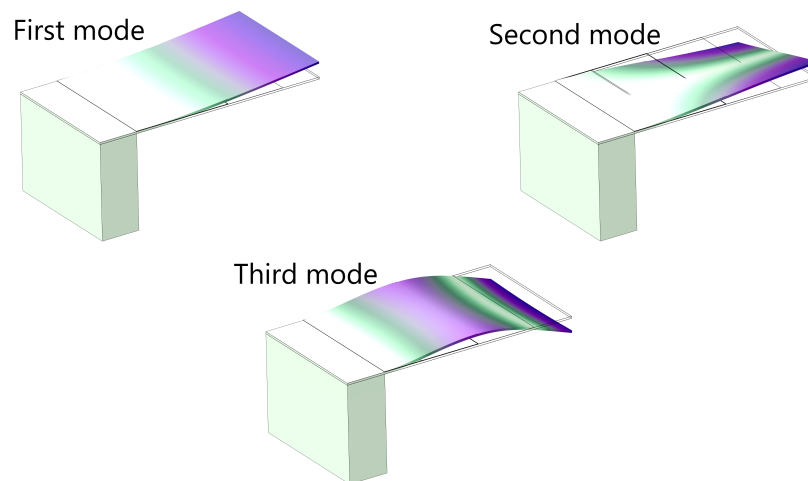

Figure 6. The cantilever beam first three mode shapes for resonance frequency obtained from eigenfrequency study around 10 kHz. The first mode shape is identical to the cantilever simple bending due to the piezoelectric effect.
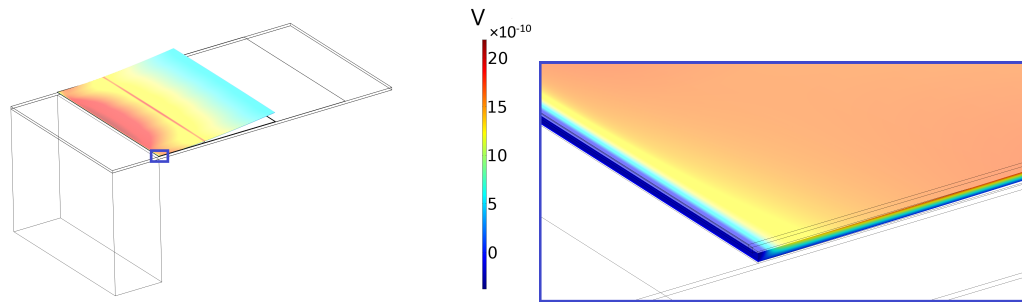
Figure 7. The piezoelectric material electric potential distribution due to the cantilever beam first mode resonance frequency.

The first three resonance modes for the optimum resonance frequency output analyzed, but the first one is the most relevant for this application. Table 2 illustrates how different piezoelectric layers and electrode materials influence the resulting frequency measurement. In the table, for the electrode layer simulation, the fixed piezoelectric material is the AlN, while for the piezoelectric material simulation, the fixed electrode layer is Au. Other aspects such as electrical capacitance losses and higher needed driving voltage depend on the piezoelectric layer material. Accordingly, aluminium nitride is the material with the most suitable electrical characteristics. This material also has the highest resonance frequency response (due to stiffness properties) and is therefore qualified as the material with the best electrical and mechanical properties.

We proceed to the next step by sweeping the width dimension for a cantilever's fixed-length simulating the structure's eigenfrequency. From the width versus frequency curve in Figure 8a, the width does not affect the first mode frequency. However, the second mode frequency gradually decreases with increased width. For the third mode, the trend is similar except for width from 600–1500 µm, where the frequency remains approximately constant. By fixing the width to 1000 µm, a parametric sweep performed on the cantilever's length, and Figure 8b shows the result. From Figure 8b, all the three modes frequencies are decreasing with the increase of length. Furthermore, the cantilever's optimum length for the desired frequency (10–12 kHz) range highlighted in the pink colour from 1800–1900 µm. From the length sweep, a strong inverse relationship observed between the length and the frequency up to 2500 µm. From that point on, the change in frequency is minimal.

Table 2. Simulation results using initial parameters for different piezoelectric material and electrode layer, the first mode result for different materials is in close range with respect to desired frequency.

Material		Resonance Frequency in kHz		
		1st Mode	2nd Mode	3rd Mode
Piezoelectric Material	AlN	12.422	39.498	63.899
	PZT-5H	11.148	36.43	58.811
	ZnO	11.562	37.275	60.667
Electrode layer	Au	12.422	39.498	63.899
	Mo	12.368	39.151	65.46
	Cu	12.134	37.946	62.039
	Al	12.395	38.841	62.898

After establishing the width and length effect on the cantilever beam resonance frequency, the next step is to simulate for the various layer thicknesses. For this simulation, a cantilever length of 1500 µm and a width of 1100 µm considered for comparison purposes with the fabricated cantilever. In Figure 9a, the first mode frequency plotted for a fixed cantilever thickness of 14 µm and an electrode thickness of 0.2 µm. From the figure, the layer thickness is directly proportional to the frequency. Out of four layers, the piezoelectric layer shows a strong effect, around 1.5 kHz for change of thickness from 0.5 µm to 1.2 µm, compared to others. Aluminium contact has the least effect of around 0.33 kHz change for a

thickness from 0.2 µm to 1 µm change. For the same change of thickness, silicon nitride and silicon oxide layers has slightly above 0.5 kHz in the first mode. From this plot, we can deduce that having a constant and precise thickness of layers, particularly for piezoelectric material, affect the outcome of the cantilever beam resonance frequency.
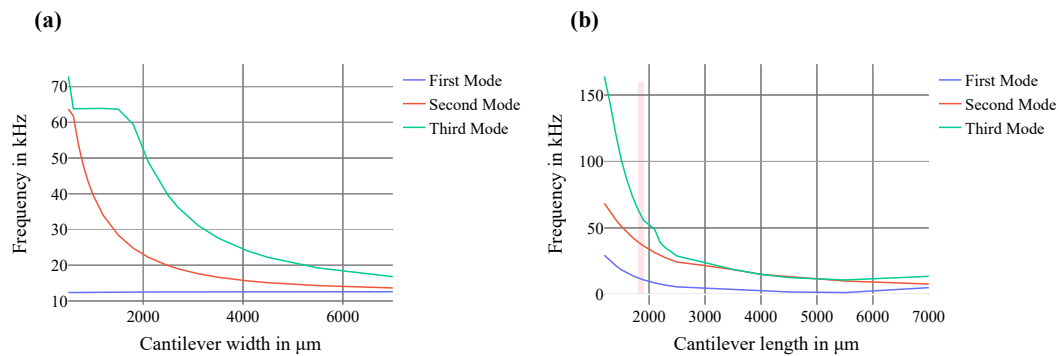
(a)

(b)

Figure 8. (**a**) Resonance frequencies versus cantilever beam width, showing the width does not affect the first mode between 500–7000 µm. (**b**) Resonance frequencies versus cantilever beam length, showing the length has a strong effect between 1000–2000 µm.
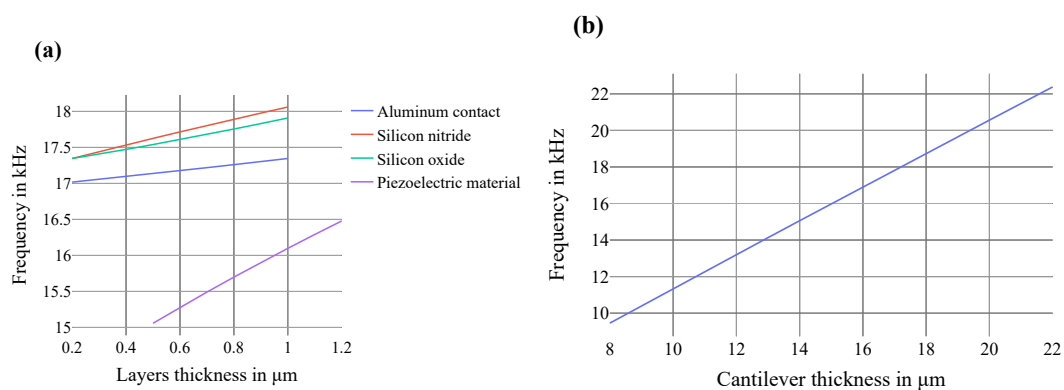
(b)

(a)

Figure 9. (**a**) Different layers thickness versus the cantilever beam first mode resonance frequency, showing the layers thickness linear effect on the frequency. (**b**) Cantilever beam thickness versus the cantilever beam first mode resonance frequency, showing the beam thickness linear effect on the frequency.

Taking the lowest value of the layer thickness from Figure 9a, since the desired frequency range is closer at lower thickness values, the cantilever thickness's effect on the first mode resonance frequency simulated. The plot in Figure 9b shows that the cantilever thickness is directly proportional to the first mode frequency, and 8 to 10.5 µm thickness shows the desired frequency range. The cantilever's thickness shows a substantial effect on the first mode frequency, implying the importance of having controlled value for optimum frequency range. From the above result, cantilever length, piezoelectric material thickness, and cantilever thickness have a significant influence in obtaining optimum frequency range. For having the desired range of frequency, the cantilever beam length lower than 1800 µm, piezoelectric material thickness and cantilever thickness should be in the lower end of the simulation range.

Using the input from the previous investigations to define the bounds of geometric parameters, we proceed to the cantiliver beam geometry optimization. First, we optimized the model for the desired frequency of 11 kHz using the different layers thicknesses default values from Table 1. The controlling variables of width = [500 µm, 1500 µm] and length = [1000 µm, 2000 µm] used to minimize the objective function in Equation (3). The optimization gave the width of 1087.4 µm and the length of 1890.8 µm.

The corresponding frequency for optimized geometric parameters is 11.002 kHz. Finally, we optimized the whole geometric parameters for the desired frequency, and the result listed in the Table 3. For the optimized thickness of different layers, the optimum length significantly lowered compared to the default values. From the result we can deduce that controlling the thicknesses of layers is essential to define the optimum cantilever beam length. Hence, the appropriate cantilever beam length dimension can be determined for a given thicknesses of layers during fabrication process to obtain optimum resonance frequency.

Table 3. Optimization result for the cantilever beam geometric parameters using BOBYQA algorithm.

Parameter	Bound (lb and ub)	Optimised Result
Cantilever length	[1000 µm, 2000 µm]	1508.9 µm
Cantilever width	[500 µm, 1500 µm]	1004.5 µm
Cantilever body thickness	[8 µm, 22 µm]	8 µm
Piezoelectric layer thickness	[0.5 µm, 1.5 µm]	0.866 µm
Silicon oxide layer thickness	[0.2 µm, 1 µm]	0.733 µm
Aluminium contact layer thickness	[0.2 µm, 1 µm]	1 µm
Silicon nitride layer thickness	[0.2 µm, 1 µm]	0.4245 µm

For this application a cantilever batch with reasonable resonance frequencies (between 10 and 12 kHz) produced. Figure 10a is the cantilever chip picture accommodated on a printed circuit board with an electrical connection to the top and bottom electrode, while Figure 10b shows how the cantilever is attached to a custom-made impedance analyzer, which actuates and reads the feedback signal from the piezoelectric layer. Figure 10c shows the parts assembled into a hand-held electronic nose, which can measure the amount of cadaverine emitted from the piece of meat. The corresponding custom driving circuit details and the device can be found in reference [27].
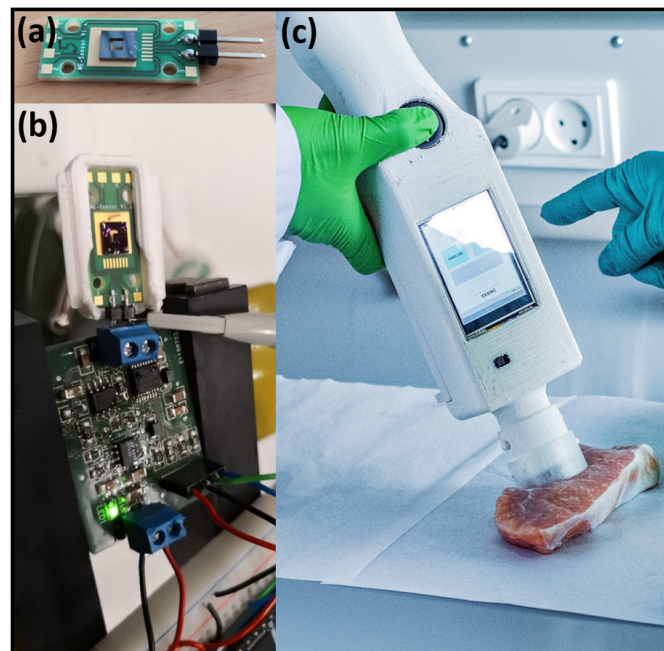

Figure 10. (**a**) Fabricated cantilever. (**b**) Cantilever attached to custom-made impedance analyzer and (**c**) Cantilever on a hand-held electronic nose.

The fabricated cantilevers resonance frequencies are measured with the impedance analyzer and found to be 10.18 kHz, which is comparable with the values obtained for the cantilever thickness range of 8 to 10.5 µm. The cantilevers response to mass added was measured by applying different masses to the cantilever and measuring the resultant resonant frequency (see Figure 11). The resonance frequency

found to reduce linearly by 3.8 kHz per mg added. Then the cantilevers were functionalized with a cadaverine binder, as described in a previous work [23–25] and exposed to tuna pieces [27]. Figure 12 shows the shift in resonance frequency when exposed to tuna pieces with different ages. As seen in the figure, the resonance frequency shift (and therefore cadaverine concentration) is increasing as expected, based on cadaverine concentration for fish at different age [7,8]. Notice that small shifts down to 0.2 kHz are successfully measured with this electronic nose, demonstrating high sensitivity for gas sensing. Detail description about our sensitivity studies found in [25]. This measurement demonstrates that the cantilevers optimized resonance frequencies work very well for cadaverine detection.
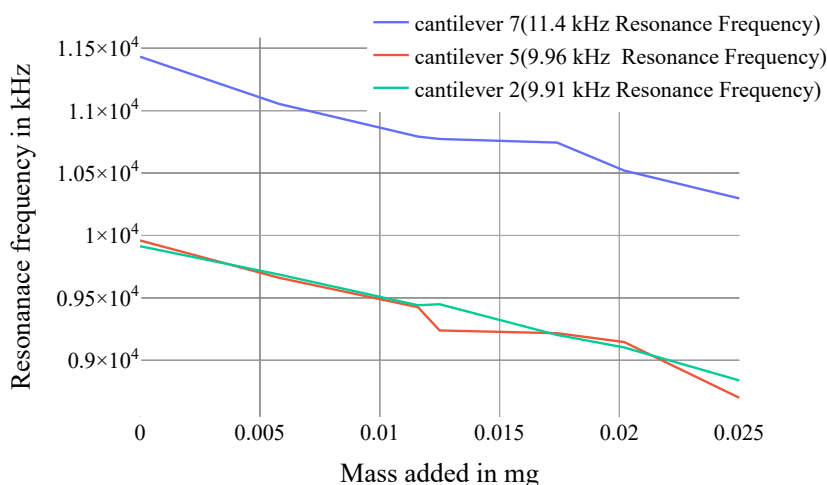

Figure 11. Change in resonance frequency with mass added to three different cantilevers.
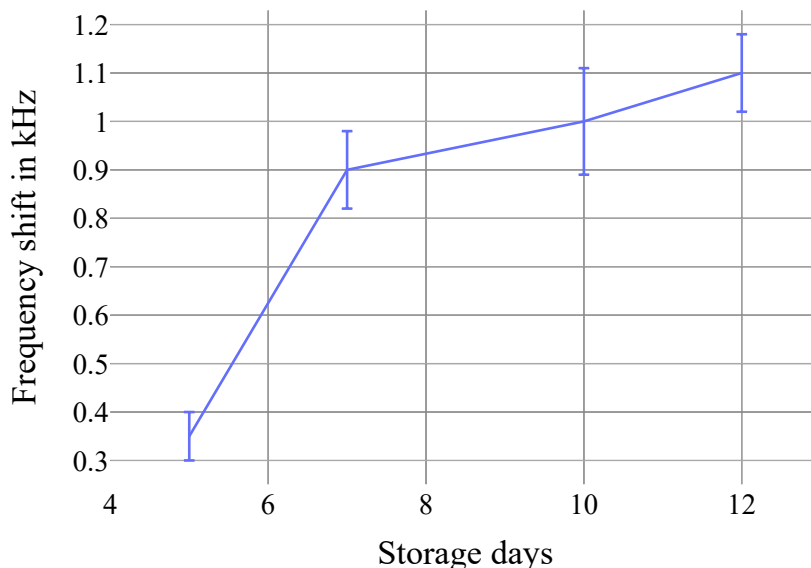

Figure 12. The shift in resonance frequency when exposed to tuna pieces with different ages, the error bars denote the shift in standard deviation.

Finally, the cantilevers morphology characterized, using ion-beam microscopy and X-ray nano tomography. Figure 13 shows both cross-section (He-ion microscopy image) and top view (X-ray image). One can observe a good layer homogeneity and expected dimensions. Cadaverine residues are observed binding on top of the cantilever.
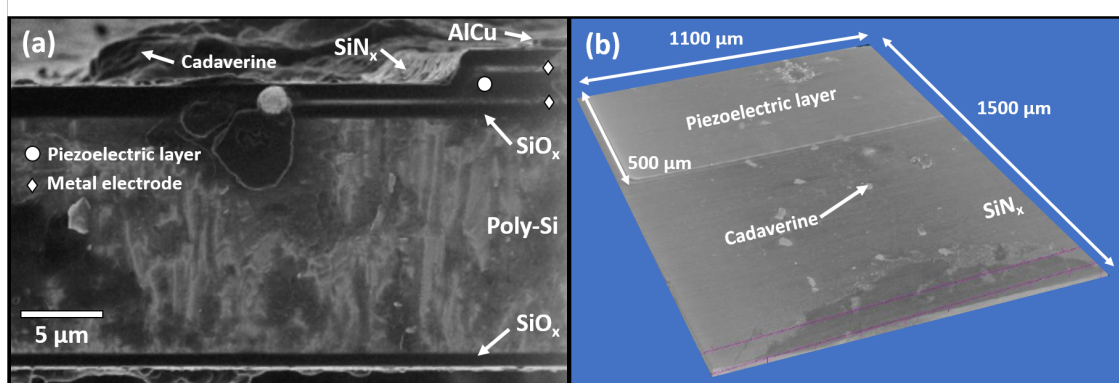
Figure 13. (**a**) Ion-beam microscopy image of cantilever cross-section, showing the different material layer thicknesses. (**b**) X-ray nanotomography top view of the cantilever, showing the material dimensions. Cadaverine spots can be observed in both images.

4. Conclusions

Expiration date determination of meat and fish products by producers are done in an indirect way, which, due to safety margin implementation, lead to a significant waste of these products through the value chain. Here, an electronic nose presented which can determine the concentration of a meat ageing biomarker (cadaverine) whereby offering producers a more direct way to determine expiration date, adding less safety margin and therefore, reducing waste. Optimum dimensions calculated for a piezoelectric cantilever via finite element analysis simulations. As a result, the cantilever beam length showed significant effect on the cantilever resonance frequency in combination with the cantilever and piezoelectric material thickness. During the fabrication process, having the minimum cantilever beam and piezoelectric material thickness could result in delivering the desired frequency range for lower cantilever length. In future work, we will calibrate the sensor output data with known cadaverine levels for a different types of meat and correlate that with the bacterial count, determining safe cadaverine threshold for consumption, which can be obtained by the sensor.

Author Contributions: Conceptualization, R.d.O.H.; methodology, M.T.K., J.M.C.D. and L.N.; software, M.T.K.; validation, J.A. and R.d.O.H.; formal analysis, M.T.K.; investigation, L.N.; resources, R.d.O.H., J.H., H.-G.R. and J.A.; data curation, M.T.K. and L.N.; writing—original draft preparation, J.M.C.D. and M.T.K.; writing—review and editing, J.A. and R.d.O.H.; visualization, M.T.K.; supervision, R.d.O.H. and J.A.; project administration, J.H., F.N., F.L., H.-G.R., J.A. and R.d.O.H. All authors have read and agreed to the published version of the manuscript.

Conflicts of Interest: The authors declare no conflict of interest.

References

1. Clune, S.; Crossin, E.; Verghese, K. Systematic review of greenhouse gas emissions for different fresh food categories. *J. Clean. Prod.* **2017**, *140*, 766–783. [CrossRef]
2. Quested, T.; Murphy, L. *Household Food and Drink Waste: A Product Focus*; Waste and Resources Action Programme: Banbury, UK, 2014. ISBN 978-1-84405-469-5.
3. Andrew, J. *Market Study on Date Marking and other Information Provided on Food Labels and Food Waste Prevention*; Publications Office of the EU: Luxembourg, 2018. [CrossRef]
4. Pircher, A.; Bauer, F.; Paulsen, P. Formation of cadaverine, histamine, putrescine and tyramine by bacteria isolated from meat, fermented sausages and cheeses. *Eur. Food Res. Technol.* **2006**, *226*, 225–231. [CrossRef]

5.   Edwards, R.; Dainty, R.; Hibbard, C. Putrescine and cadaverine formation in vacuum packed beef. *J. Appl. Bacteriol.* **1985**, *58*, 13–19. [CrossRef]

6.   Laursen, B.; Byrne, D.; Kirkegaard, J.; Leisner, J. Lactic acid bacteria associated with a heat-processed pork product and sources of variation affecting chemical indices of spoilage and sensory characteristics. *J. Appl. Microbiol.* **2009**, *106*, 543–553. [CrossRef] [PubMed]

7.   Gui, M.; Binzhao; Song, J.; Zhang, Z.; Hui, P.; Li, P. Biogenic amines formation, nucleotide degradation and TVB-N accumulation of vacuum-packed minced sturgeon (*Acipenser schrencki*) stored at 4 °C and their relation to microbiological attributes. *J. Sci. Food Agric.* **2014**, *94*, 2057–2063. [CrossRef] [PubMed]

8.   Vinci, G.; Antonelli, M. Biogenic amines: Quality index of freshness in red and white meat. *Food Control* **2002**, *13*, 519–524. [CrossRef]

9.   Quality indices for canned skipjack tuna: Correlation of sensory attributes with chemical indices. *Off. Ication Inst. Food Technol.* **1992**, *57*, 1112–1115.

10.   Emborg, J.; Laursen, B.; Rathjen, T.; Dalgaard, P. Microbial spoilage and formation of biogenic amines in fresh and thawed modified atmosphere-packed salmon (*Salmo salar*) at 2 °C. *J. Appl. Microbiol.* **2002**, *92*, 790–799. [CrossRef]

11.   Stolzenbach, S.; Leisner, J.J.; Byrne, D.V. Sensory shelf life determination of a processed meat product 'rullepølse' and microbial metabolites as potential indicators. *Meat Sci.* **2009**, *83*, 285–292. [CrossRef]

12.   Leuschner, R.G.; Kurihara, R.; Hammes, W.P. Formation of biogenic amines by proteolytic enterococci during cheese ripening. *J. Sci. Food Agric.* **1999**, *79*, 1141–1144. [CrossRef]

13.   Nishikawa, H.; Tabata, T.; Kitani, S. Simple Detection Method of Biogenic Amines in Decomposed Fish by Intramolecular Excimer Fluorescence. *Food Nutr. Sci.* **2012**, *3*, 1020–1026. [CrossRef]

14.   Almeida, C.; Fernandes, J.; Cunha, S. A novel dispersive liquid–liquid microextraction (DLLME) gas chromatography-mass spectrometry (GC–MS) method for the determination of eighteen biogenic amines in beer. *Food Control* **2012**, *25*, 380–388. [CrossRef]

15.   Hidayat, S.N.; Triyana, K.; Fauzan, I.; Julian, T.; Lelono, D.; Yusuf, Y.; Ngadiman, N.; Veloso, A.C.; Peres, A.M. The Electronic Nose Coupled with Chemometric Tools for Discriminating the Quality of Black Tea Samples In Situ. *Chemosensors* **2019**, *7*, 29. [CrossRef]

16.   Yang, T.; Tian, F.; Covington, J.A.; Xu, F.; Xu, Y.; Jiang, A.; Qian, J.; Liu, R.; Wang, Z.; Huang, Y. Resistance-Capacitance Gas Sensor Based on Fractal Geometry. *Chemosensors* **2019**, *7*, 31. [CrossRef]

17.   da Costa Arca, V.; Peres, A.M.; Machado, A.A.; Bona, E.; Dias, L.G. Sugars' Quantifications Using a Potentiometric Electronic Tongue with Cross-Selective Sensors: Influence of an Ionic Background. *Chemosensors* **2019**, *7*, 43. [CrossRef]

18.   da Silva, A.; Braunger, M.L.; Neris Coutinho, M.A.; Rios do Amaral, L.; Rodrigues, V.; Riul, A. 3D-Printed Graphene Electrodes Applied in an Impedimetric Electronic Tongue for Soil Analysis. *Chemosensors* **2019**, *7*, 50. [CrossRef]

19.   Boisen, A.; Dohn, S.; Keller, S.S.; Schmid, S.; Tenje, M. Cantilever-like micromechanical sensors. *Rep. Prog. Phys.* **2011**, *74*, 036101. [CrossRef]

20.   Preumont, A. *Vibration Control of Active Structures*; Springer International Publishing: Cham, Switzerland, 2018. [CrossRef]

21.   Younis, M.I. *MEMS Linear and Nonlinear Statics and Dynamics*; Springer: Cham, Switzerland, 2011. [CrossRef]

22.   Homayouni-Amlashi, A.; Mohand-Ousaid, A.; Rakotondrabe, M. Analytical Modelling and Optimization of a Piezoelectric Cantilever Energy Harvester with In-Span Attachment. *Micromachines* **2020**, *11*, 591. [CrossRef]

23.   Costa, C.A.B.; Grazhdan, D.; Fiutowski, J.; Nebling, E.; Blohm, L.; Lofink, F.; Rubahn, H.G.; de Oliveira Hansen, R. Meat and fish freshness evaluation by functionalized cantilever-based biosensors. *Microsyst. Technol.* **2019**, *26*, 867–871. [CrossRef]

24.   Wang, Y.; Sobolewska, E.K.; Fiutowski, J.; Rubahn, H.G.; de Oliveira Hansen, R.; Albers, J.; Nebling, E.; Wagner, B.; Benecke, W.; Hansen, R.D.O. Functionalizing micro-cantilevers for meat degradation measurements. In Proceedings of the 2016 Symposium on Design, Test, Integration and Packaging of MEMS/MOEMS (DTIP), Budapest, Hungary, 30 May–2 June 2016. [CrossRef]

25.   Wang, Y.; Costa, C.A.B.; Sobolewska, E.K.; Fiutowski, J.; Brehm, R.; Albers, J.; Nebling, E.; Lofink, F.; Wagner, B.; Benecke, W.; et al. Micro-cantilevers for optical sensing of biogenic amines. *Microsyst. Technol.* **2017**, *24*, 363–369. [CrossRef]

26. Powell, M. *The BOBYQA Algorithm for Bound Constrained Optimization without Derivatives*; Technical Report; Department of Applied Mathematics and Theoretical Physics: Cambridge, UK, 2009.

27. Alexi, N.; Hvam, J.; Lund, B.W.; Nsubuga, L.; de Oliveira Hansen, R.M.; Thamsborg, K.; Lofink, F.; Byrne, D.V.; Leisner, J.J. Potential of novel cadaverine biosensor technology to predict shelf life of chilled yellowfin tuna (*Thunnus albacares*). *Food Control* **2020**, *119*, 107458. [CrossRef]